Fourier Optical Imaging of Discrete Stimuli in Primate Somatosensory Cortex

By

Jeremy Winberry

Thesis

Submitted to the Faculty of the

Graduate School of Vanderbilt University

in partial fulfillment of the requirements

for the degree of

MASTER OF SCIENCE

in

Neuroscience

May, 2014

Nashville, Tennessee

Approved:

Troy Hackett, Ph.D.

Peter Konrad, M.D., Ph.D.

Anna Roe, Ph.D.

Mark Wallace, Ph.D.

TABLE OF CONTENTS

LIST OF FIGURES

Chapter I

Introduction

Neocortex is a thin, six-layered structure encompassing most of the cerebral hemispheres of the forebrain. While cortex looks homogeneous, local specializations arise from differential projections from thalamus and other cortical areas, as well as from local cytoarchitectural differences. The functional specializations of cortex came to light thanks to neurological studies of patients with brain lesions that produced very specific behavioral deficits, such as Broca's area lesions that rendered patients unable to produce spoken words (Broca, 1861). The possibility of mapping the cerebral cortex into functional areas was realized by David Ferrier, who electrically stimulated the exposed cortex of rabbits, cats, and dogs to map motor cortex (Ferrier, 1873). Ferrier also noticed that application of strong electric currents to cortex generated strong, erratic movements spreading along the contralateral side of the body. This was recognized as a possible explanation for Jacksonian seizures. Neurosurgeons became interested in functional mapping of motor cortex upon the realization that disturbances in the motor map could be used to localize brain tumors. Intraoperative cortical stimulation progressed through the first half of the 20th century, culminating in the Montreal procedure of Jasper and Penfield (Penfield and Jasper, 1954). Use of local anesthesia in awake patients allowed neurosurgeons to use electrical stimulation to map sensory areas beyond motor cortex. Coupled with intraoperative electrocorticography (ECoG), pioneered by neurosurgeon Foerster (Piotrowska and Winkler, 2007), Penfield and Jasper could distinguish eloquent from epileptogenic cortex.

Findings from macroelectrode stimulation and ECoG recording sites helped to assign functions to the anatomical divisions posited by Brodmann and others. However, aside from gross maps such as somatotopy, these methods did not have the spatial resolution to study the functional architecture of individual areas. Extracellular microelectrode recordings in animals started gaining popularity in research in the 1950's. It was here that the columnar structure of cortex was revealed (Hubel and Wiesel, 1962; Mountcastle, 1957; Powell and Mountcastle, 1959). The columnar organization of functional responses, such as responses to oriented stimuli, suggested another level of organization: that of discrete, clustered cortical columns. Unfortunately, while extracellular microelectrode recordings provided very high spatial resolution, they are not efficient at mapping columnar organization across a cortical area.

Optical imaging methods soon filled the gap left by extracellular electrophysiology, and domain-level functional maps were described with voltage-sensitive dye imaging (VSDI) (Blasdel and Salama, 1986) and intrinsic optical imaging (OIS) (Bonhoeffer and Grinvald, 1991; Ts'o et al., 2001). Unlike fMRI, these techniques are capable of mapping small domain-level structures such as orientation pinwheels in primary visual cortex (VI). However, VSDI requires staining the brain with a dye, and experiments are limited by the time it takes to quench the dye. OIS can be recorded for hours or days,

thanks to its reliance on the endogenous hemodynamic response. Unlike fMRI, which uses BOLD signal based on a rush of oxygenated blood delivered to active cortical regions that peaks by 10 seconds after cortical activation, OIS uses the initial dip signal based on the local consumption of oxygen 0-3 seconds after cortical activation. This, coupled with the smaller effective size of pixels compared to voxels explains why OIS can be used to study domain-level cortical structures whereas fMRI cannot.

However, OIS does have several significant shortcomings. The amplitude of the initial dip is a fraction of a percent change that can be drowned out by physiological noise such as heart rate and respiration. Measures taken to reduce noise and ensure a stabile baseline include syncing to respiration and heart rate, averaging many trials, collecting blank trials, and setting long inter-trial intervals. These measures add extra time to the experiment and increase signal susceptibility to cognitive/motivational changes in awake animals or physiological fluctuations in anesthetized animals that can occur over time.

Kalatsky and Stryker (2003) developed a more efficient intrinsic optical imaging method, whereby continuous, periodic stimulation and continuous image recording replaced the typical trial-based episodic imaging of OIS. Careful selection of the stimulus frequency makes it possible to separate with Fourier decomposition analysis the stimulus response from common physiological noise frequencies such as heart rate, respiration rate, and vasomotion. Furthermore, the technique requires neither blank conditions nor inter-stimulus intervals. The end result is a less noisy, functional topographic map collected in a fraction of the time required for episodic OIS. The method has successfully been applied to rodent and cat visual cortex, and to rat and ferret auditory cortex (Kalatsky et al., 2005; Kalatsky and Stryker, 2003; Nelken et al., 2004). While this approach has been used in human fMRI studies (Boynton et al., 1996; DeYoe et al., 1996; Engel et al., 1997; 1994; Sereno et al., 1995), to date, no examples of this technique have been published in non-human primates (NHP) or in mapping monkey somatosensory finger topography.

Tactile sensation informs us of our physical interactions with objects around us, but how such information is organized and processed in primary somatosensory cortex (SI) is still poorly understood. The only known functional organizations in SI correspond to somatotopy (Chen et al., 2001; Nelson and Kaas, 1981; Paul et al., 1972a; 1972b; Pons et al., 1987) and cutaneous receptor modality (Friedman et al., 2004). With Fourier OIS, it may be possible to map in SI continuously variable somatosensory stimuli as has been achieved in the visual system with orientation and direction (Vanni et al., 2010a). With prospects of faster experiment time, decreased noise, and new experimental paradigms that could push primate somatosensory OIS forward, I decided to develop techniques for Fourier optical imaging and apply them to the squirrel monkey SI finger representation. To evaluate this approach, I examined SI finger topography using continuous OIS of discrete, periodic finger stimulation and a Fourier decomposition analysis in the anesthetized squirrel monkey. Maps generated using the continuous OIS approach compared favorably to known somatotopy and episodic OIS maps with significant time savings. I also expanded upon the Fourier decomposition approach to generate images reflecting statistical signal significance rather than magnitude as an independent means of confirming the resulting image maps.

Chapter II

Methods

Surgical Procedures

Squirrel Monkeys (n=7) were sedated with ketamine (10 mg/kg), anesthetized with isoflurane and artificially ventilated. Animals were placed on a heating blanket, secured in a stereotaxic frame, and monitored continuously for end-tidal CO_2, heart-rate, and temperature. A craniotomy and durotomy were performed to expose the hand area of primary somatosensory cortex. The brain was stabilized with 4% agar and a cover glass provided a clear imaging window. All procedures were conducted in accordance with National Institutes of Health guidelines and were approved by the Vanderbilt University Animal Care and Use Committee.

Somatosensory Stimuli

The contralateral forearm and hand were shaved and secured outstretched in a supine position. Two mm diameter probes, attached to piezoceramic actuators (Noliac A/S, Denmark) were placed with a slight indention (app. 500 microns) on the palmar side of a distal phalanx of one, two, or three digits. Tactile stimulation of an individual digit consisted of a train of square wave pulses delivered at 8 Hz, with each pulse having a displacement of 250 μm and lasting 20 ms. Stimulation was periodic, with a 12 s period wherein D2, D3, and D4 tips were sequentially stimulated for two seconds with a two second ISI between each stimulus. Stimuli such as this have been shown to be effective at eliciting cortical neuronal responses as assessed with electrophysiology and optical imaging (e.g. Chen et al., 2003; Friedman et al., 2008).

Optical Imaging

Images of diffuse reflected light, corresponding to the intrinsic hemodynamic signal, were obtained through a CCD video camera (512 x 512 or 256 x 256 pixels, 8 x 8 mm field of view) connected to an imaging system (Imager 3001, Optical Imaging Ltd., Israel; or NeuroCCD, Redshirt Imaging, USA). Cortex was illuminated with red light (632 nm) for signal acquisition and green light (578 nm) for blood vessel maps. To compare continuous image acquisition methods with traditional episodic acquisition methods, we collected functional maps with both approaches. Continuously acquired data were sampled at 10 or 25 frames per second for 10 to 30 minutes. Episodic data were sampled at 5 frames per second and 12 s per trial. A total of 57 trials were collected over 50 minutes. Both datasets were acquired in the same experimental session, under the same anesthesia and lighting conditions, and with the same imaging system.

Electrophysiology

A hydraulic microdrive (Narishigi, Japan) was used to lower 0.9 to 1.5 MΩ Parylene-C coated tungsten microelectrode (Micro Probe Inc., Gaithersburg, MD) through agar and into image-guided targeted locations of the cortex. Multi-unit activity was filtered, amplified, and played over a loudspeaker in order to allow a qualitative judgment of tactile receptive fields.

Image Analysis

All continuous image analysis was performed offline in MATLAB (The Mathworks, Nattick, MA). Images were bandpass filtered (0.08 - 2.65 mm, circular averaging) to remove high and low frequency noise. This filtering removed global artifacts that especially interfered with the phase component described below. Subsequent analysis was computed separately for each pixel. First, slow temporal artifacts corresponding to baseline drift were removed by subtracting a running average with a filter width of twice the length of the stimulus period. Then, a Fourier transform was used to obtain phase and magnitude values. Phase values and any calculations using them were kept in radians (0-2π). No spatial filtering was performed after the Fourier transform. Magnitude scale bars were thresholded from 0 to 1, and any contrast or brightness changes were only made for display images and did not alter values used in calculations. A smoothing spline of the magnitude spectrum was used to estimate the noise floor before signal to noise analysis. Signal to noise ratios were computed by dividing the magnitude at the principal frequency by the calculated noise floor. Digit selectivity values were computed by dividing the raw magnitude at the first harmonic frequency by the raw magnitude at the second harmonic frequency. This yields an effective ratio of single vs multidigit responses.

Episodic imaging was also performed offline in MATLAB. Conditions were averaged across trials. Multiple image frames were averaged to increase the signal to noise, and the percent reflectance change with respect to the first frame was calculated. Images were bandpass filtered (0.08 - 2.65 mm) to remove high and low frequency noise. For presentation, images were clipped to ± 1-2 standard deviations from the median pixel value.

Chapter III

Results

The potential of optically imaging continuously to reveal the functional cortical organization of primate cortex in response to discrete stimuli was investigated in somatosensory cortical areas of anesthetized squirrel monkeys during stimulation of distal fingertips. Stimulation was periodic, with a 12 s period during which D2, D3, and D4 tips were sequentially stimulated (8 Hz train of square wave pulses, 250 μm displacement, 20 ms per pulse) for two seconds with a two second ISI between each stimulus (Fig. 1A). As opposed to continuous visual stimuli used by others (Kalatsky and Stryker, 2003; Vanni et al., 2010a), our stimuli were discontinuous on the sensory surface (three separate digits) and discrete in temporal presentation due to ISI's between stimuli. We predicted that the cortical pattern of activity (represented in the upper panel of Fig. 1) resulting from this digit stimulation paradigm should follow the stimulation frequency and, furthermore, that cortical activity associated with different digits should have different relative phases offset by 4 seconds (2 sec digit stimulation plus ISI period, see lower panel of Fig. 1A). There should also be a lag between stimulus onset and response onset due to the lag inherent in the hemodynamic signal (time to intrinsic signal peak at 632 nm light, roughly 2-5 sec).

Fourier decomposition

Because the sequence of collected images is contiguous over time and stimuli are presented periodically, the signal from each pixel can be treated as a continuous temporal waveform and be decomposed in the frequency domain. An example of a signal timecourse during a 10 minute run (Fig. 1B, black), taken from a 50 x 50 pixel region (see Figure 6E for ROI) within the D2 fingertip representation of area 3b, contained both regular, fast variation and irregular, slow variation components. The fast variation components reflect respiration and heart beat, while the slow variation reflects vasomotion and irregular noise sources (Kalatsky and Stryker, 2003). One of the goals of the Fourier decomposition of the optical images is to separate the frequencies associated with the stimulated response from these other physiological noise signals. To achieve this, several steps are involved. First, to remove DC offsets and to compensate for slow variations in baseline reflectance that could interfere with the sinusoidality of the stimulus dependent waveform, we subtracted a running average (Fig 1B, red) calculated from the raw timecourse. This was done on a pixel by pixel basis to maintain spatial signal integrity.

After baseline subtraction, a pixel-wise Fourier decomposition of the waveform was performed in Matlab to extract target frequency information. This was checked with a simulated data set consisting of a periodic sine wave grating to confirm that signal extraction algorithm produced the expected outcome. Example magnitude plots, which plot the magnitude of the signal with respect to frequency, obtained by the Fourier decomposition of 50 x 50 pixel regions (Fig. 1C, plotted on Figure 6E) are shown for demonstration purposes in Figure 1C-E. The magnitude plot from an ROI within the D3 fingertip

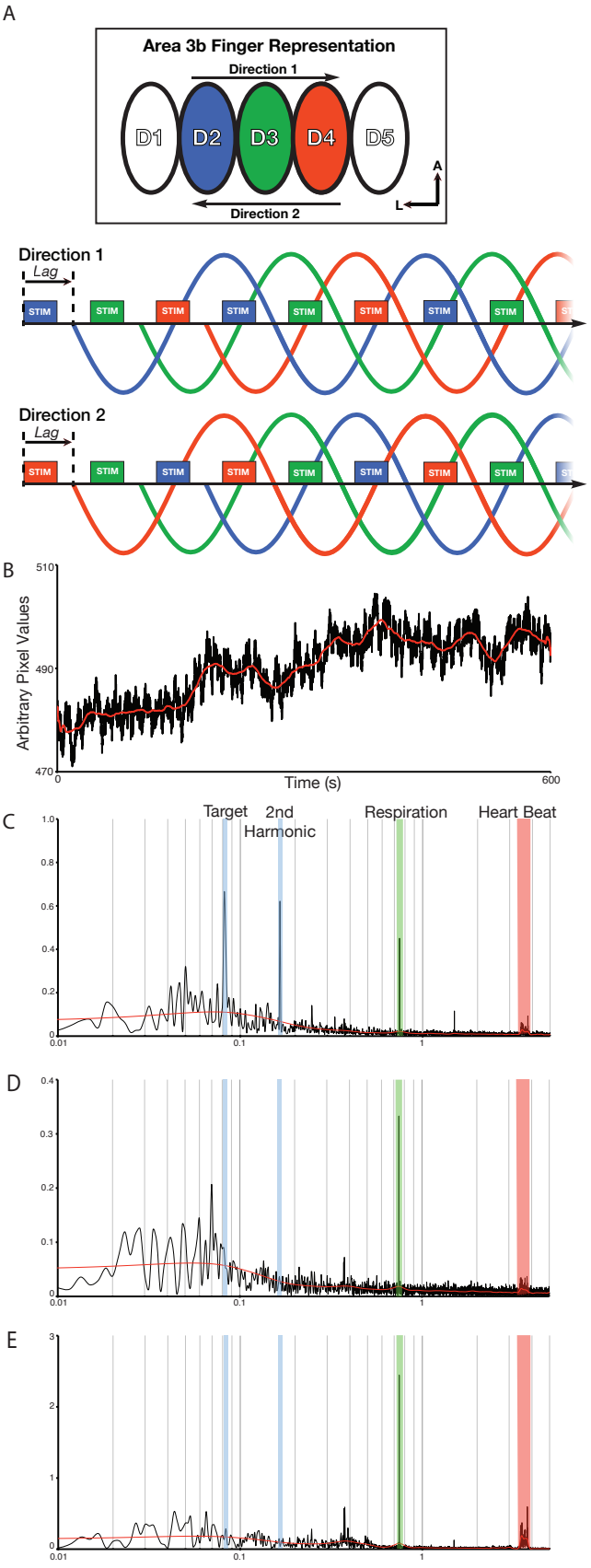
A
Area 3b Finger Representation
Direction 1
D1
D2
D3
D4
D5
A
L
Direction 2
Direction 1
Lag
STIM
Direction 2
Lag
STIM
B
Arbitrary Pixel Values
510
490
470
0
600
Time (s)
C
Target
2nd Harmonic
Respiration
Heart Beat
1.0
0.8
0.6
0.4
0.2
0
0.01
0.1
1
D
0.4
0.3
0.2
0.1
0
0.01
0.1
1
E
3
2
1
0
0.01
0.1
1

Figure 1. Periodic tactile stimulation and Fourier decomposition. A. Stimulation was periodic, with a 12 s period wherein D2, D3, and D4 tips were sequentially stimulated. Separate runs were performed for opposite stimulus orders. Cortical activity resulting from digit stimulation should repeat at the stimulation frequency, but regions of cortex responding to different digits will have different phases. Prior to pixel analysis, images were bandpass filtered (0.08 - 2.65 mm) to remove high and low frequency noise. B. A timecourse (black) during a 10 minute run from an ROI. A running average (red) was calculated from the raw timecourse to compensate for slow changes in baseline reflectance. C. Magnitude plot obtained by the Fourier decomposition of area 3b ROI (see Fig. 6E, mid-left) demonstrates signal at the stimulus frequency (0.083 Hz, blue) and its second harmonic (0.167 Hz, blue) were segregated from heart- (red) and respiration-related (green) noise. D. Magnitude plot obtained by the Fourier decomposition of area 1 ROI (see Fig 6E, lower), showing lower signal peaks at the stimulus and second harmonic frequencies than the area 3b ROI. E. Magnitude plot obtained by the Fourier decomposition of large vessel ROI (see Fig 6E, mid-right), showing high cardiovascular noise peaks at the respiration, heart rate and vasomotor (0.37 Hz) frequencies. Red lines in C-E indicated noise floor estimates.

representation in area 3b (see Figure 6E for ROI) demonstrated peaks at the stimulus (target) frequency (0.083 Hz, blue) and its second harmonic (0.167 Hz, blue). These were distinct from heart- (3.4-3.9 Hz, red) and respiration-related (0.72 Hz, green) frequencies. Artificial respiration ensured a sharp respiration-related peak that often had one or more harmonic peaks (i.e. Fig. 1C, 1.44 Hz). In an ROI taken from the D3 fingertip representation in area 1 (see Figure 6E for ROI), the target frequency and its second harmonic (Fig. 1D, blue) were reduced almost to the estimated noise floor (red curve). For this case, this reflects the smaller signal sizes that were observed in area 1 under isoflurane anesthesia (Friedman et al. 2008). Respiration- and heart-related frequencies were also present, but with diminished magnitude. A magnitude plot made from an ROI over central sulcus vessels (see Fig. 6E for ROI) showed a higher noise floor than areas 3b and 1 (Fig. 1 D-E, red curves). As expected, the respiration- and heart-related peaks were much larger than at the other sites, while the magnitude at the target frequency and its second harmonic were small with respect to the noise floor. An additional broad peak centered around 0.37 Hz demonstrated the vasomotor components of the signal. The demonstrated response magnitudes at predicted target frequency (and its harmonics) and the location specificity of the response (area 3b, area 1, vessel) indicates the Fourier approach to signal isolation is feasible in somatosensory cortex.

Magnitude and polar maps

After the Fourier transform, magnitude and phase values at the target frequency (0.083 Hz) for each pixel are used to reconstruct a magnitude map and a phase map. Magnitude maps show the amplitude of the cortical response to tactile stimulation, and phase maps show the relative timing of the cortical responses to temporally offset stimuli that share the same period. Figure 2 illustrates images of somatosensory cortex resulting from tactile stimulation of the contralateral hand. Images are shown for stimulation of fingertips D2, D3, D4 for the left hemisphere (Fig 2A,C,E,G), and D3, D2, D1 for the right

(Fig. 2B,D,F,H) hemisphere of the same brain. Blood vessel patterns from area 3b of SI are shown (Fig 2A,B).

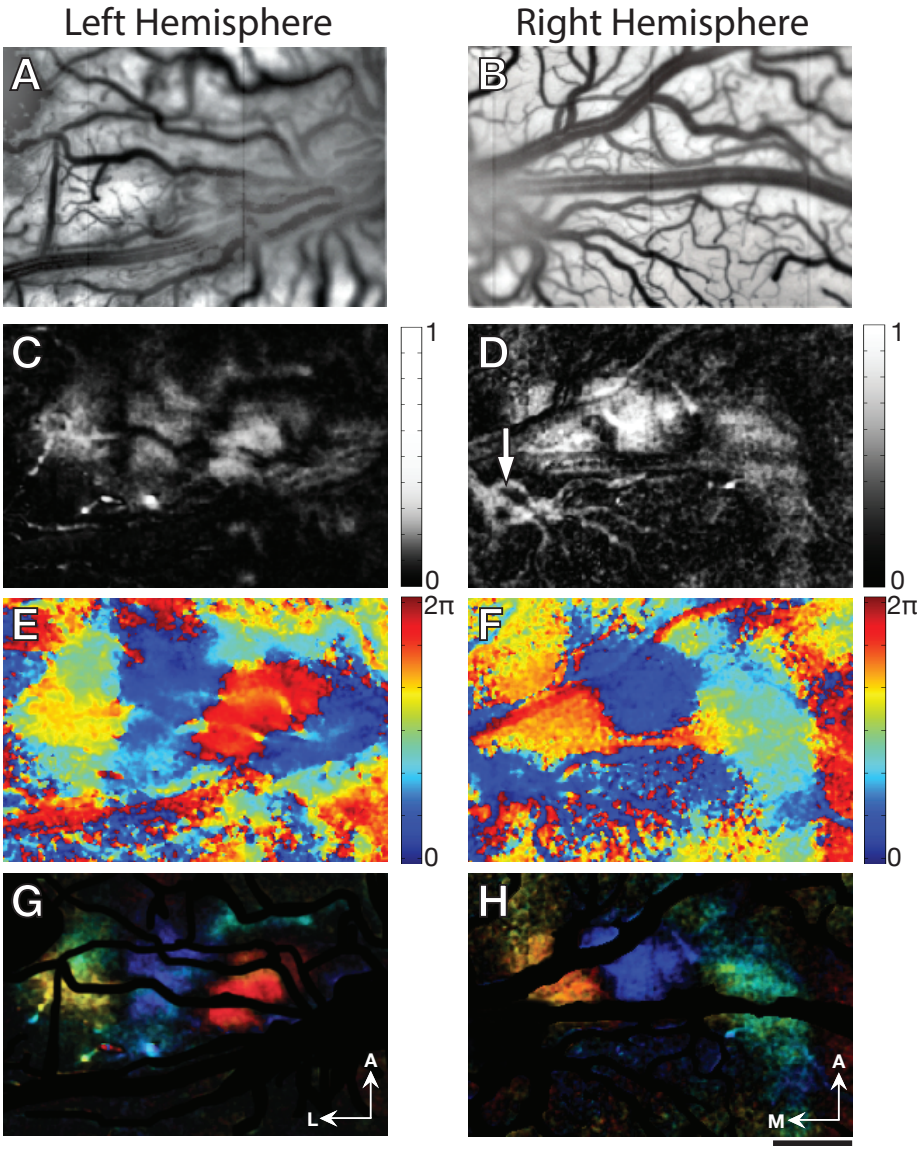

Figure 2. Reconstructed image maps generated with magnitude and phase Fourier transform values at the target frequency. A and B. Blood vessel maps of the imaging field of view for the left (Fig 2A,C,E,G) and right (Fig. 2B,D,F,H) hemispheres of the same brain. C and D. Magnitude maps showing the amplitude of the cortical response to tactile stimulation of D2, D3 and D4. E and F. Phase maps showing 3 different colored regions reflect the relative timing of the cortical responses to the 3 temporally offset stimuli. Phase measured in radians (0 to 2 pi) is independent of period length. G and H. Polar maps combining the magnitude and phase maps visualize the signal strength and its relative timing. Scale bar = 1mm. L = left, R= right, A = anterior.

The magnitude maps (Fig 2C,D) revealed three distinct regions of brightness corresponding to cortical activation to the stimulation of the three individual fingertips in area 3b, respectively (magnitude scale shown at right in D). The three digit-activated regions were ~1 mm wide, similar to electrophysiologically mapped 3b digit topography (Sur et al., 1982) and to episodic OIS maps (Chen et al., 2001). Note that magnitude maps often showed strong signal over large blood vessels (Fig 2D, arrow). Signal centered over large vessels maintained the tree branch-like appearance of the blood vessels and were easily identified by referencing to the vessel map.

The phase maps showed three central phase-locked regions with sharp borders (Fig. 2C,D), with each region dominated by a different range of phase values (in radians, phase scale shown at right in F). These color-coded maps revealed the presence of three distinct responses of different latency (separated by roughly 4 sec) within a stimulation period. Non-activated regions in the magnitude maps appear grainy and noisy in the phase maps, as the phase in these regions did not correlate in a coherent fashion relative to the stimulation frequency and was only being modulated by background noise.

By combining magnitude and phase maps into a polar map, it is possible to visualize the target frequency signal strength and its relative timing. [Note: large vessels have been masked out for clarity] In polar maps, response phase is illustrated with color and response intensity with color saturation. These polar maps (Fig. 2E,F) nicely reveal three regions with distinct phases. These phases correspond to the somatotopic locations of the distal finger pads D2 (yellow/green), D3 (blue), and D4 (orange/red) in area 3b left (Fig. 2A, C, E) and right (Fig 2. B, D, F) hemispheres.

Correction for hemodynamic lag

While these maps reflect the relative phases of activation, there is no correction for the hemodynamic lag. Two methods can be applied to incorporate the hemodynamic lag in the measured phase. In the first method, the hemodynamic lag can be removed using a reversed stimulus sequence data collection strategy (Kalatsky and Stryker, 2003). Imaging data are collected with the stimuli presented in one sequence for one recording session and in the reverse sequence for another session. Fig 3A illustrates the polar map obtained by the stimulation sequence D4, D3, D2. Fig 3B illustrates the polar map obtained by the stimulation sequence D2, D3, D4.

At each pixel, subtraction (see Eq. 1) of the observed phase of the former, consisting of stimulus phase plus hemodynamic response delay (θ+d), minus the latter, consisting of reversed stimulus phase

$$\frac{(\theta + d) - (2\pi - \theta + d)}{2} = \theta_{corrected} \quad \text{(Eq. 1)}$$

plus delay (2π-θ+d), followed by division by two produces the stimulus phase (θ) of the original phase map (Fig 3C). This is because the hemodynamic response delays in the opposite sequences cancel out

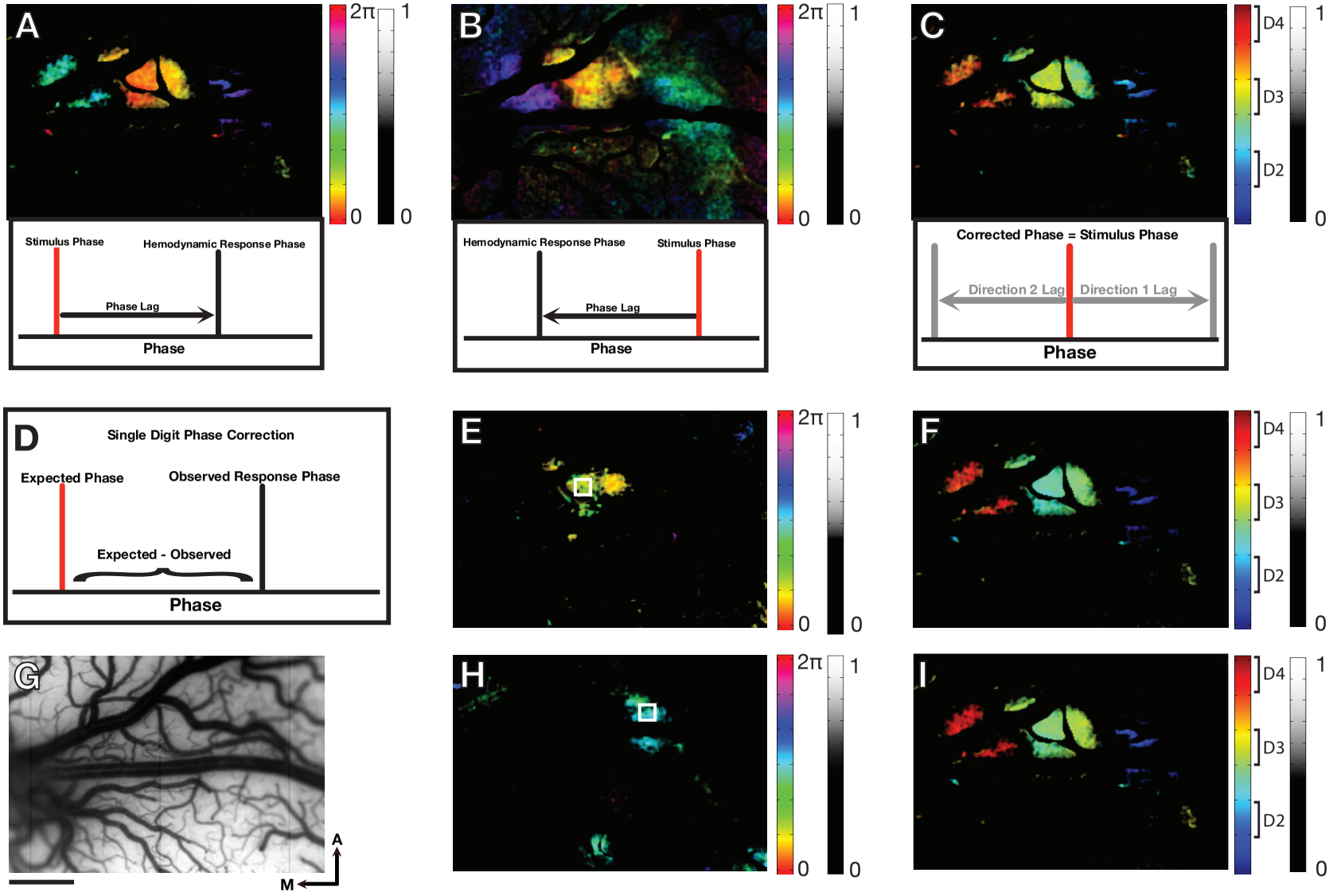
A
2π
1
0
0
Stimulus Phase
Hemodynamic Response Phase
Phase Lag
Phase
B
2π
1
0
0
Hemodynamic Response Phase
Stimulus Phase
Phase Lag
Phase
C
D4
D3
D2
1
0
Corrected Phase = Stimulus Phase
Direction 2 Lag
Direction 1 Lag
Phase
D
Single Digit Phase Correction
Expected Phase
Observed Response Phase
Expected - Observed
Phase
E
2π
1
0
0
F
D4
D3
D2
1
0
G
A
M
H
2π
1
0
0
I
D4
D3
D2
1
0

Figure 3. Phase lag correction of image maps. A. Polar map obtained by the stimulation sequence D4, D3, D2. B. Polar map obtained by the stimulation sequence D2, D3, D4. C. Lag corrected phase map. Hemodynamic response delays were cancelled out by subtraction of the phase value at each pixel and dividing by 2 for the 2 opposite sequences (A and B). D. The delay is calculated as the expected phase minus the observed phase and assumes spatial homogeneity in the lag of the hemodynamic response. E. Phase map showing the region responding to discrete D3 stimulation used to calculate the phase lag. F. Lag corrected phase map where the constant lag calculated from E was subtracted from each pixel of the map (A). G. Blood vessel map of the imaging field of view. H and I. Phase map showing the region responding to discrete D4 stimulation and the subsequent lag correction of map in A. Both methods generate corrected phase maps that demonstrate the correct digit sequence for D2, D3 and D4. Scale bar = 1 mm. M = medial. A = anterior.

(Fig. 3C, lower panel), leaving the true stimulus phase. This method of phase correction assumes independence of stimulus order.

A second method uses a single discrete stimulus with known timing within a period; this is compared to the lagged phase of a measured cortical response (Fig. 3D). In this case, we used 2 s of single-D3 digit stimulation in the same 12 s period as before. The observed phase was calculated (see Eq. 2) by measuring the average phase in a region responding to D3 stimulation (Fig. 3E white box). The delay (d) is calculated as the expected phase (θ) minus the observed phase (θ+d). The result (-d), in

$$(\theta - (\theta + d))_{ROI} + (\theta + d)_{pixel} = \theta_{corrected} \quad \text{(Eq. 2)}$$

radians, is added to the observed phase of every pixel of the map in Fig. 3A to give a corrected phase map (Fig.3F). The digit used for phase correction did not matter, as an ROI from D2 in a discrete D2 stimulation session (Fig. 3H white box) produced a comparable phase-correction of Fig. 3A (Fig. 3I). This approach assumes spatial homogeneity in the hemodynamic response so that the phase of the ROI can be applied to all pixels. Both phase correction methods generate phase maps that demonstrate the correct digit sequence for D2, D3 and D4. However, stimulus reversal is done for each stimulus set, whereas the discrete stimulus correction is collected once and provides a constant phase correction value across differing stimulus sets.

Functional magnitude borders

One of the striking observations of discrete 3-digit stimulation was that sharp borders were seen between digits in the polar maps (Fig. 4A, arrows). This differs from episodic OIS (Chen et al., 2009; Friedman et al., 2008) and BOLD fMRI (Chen et al., 2007) where overlapping activations by adjacent digit stimulations are common and response amplitude does not drop sharply at the border between adjacent digit representations. If the high-magnitude regions were really restricted to the somatotopic location corresponding to the stimulus, it would be expected that activation would be restricted to the

distal phalanx representation. To determine whether there are sharp functional borders within a digit representation, we stimulated along a digit at the centers of the proximal, middle, and distal phalanges using the same 12s period and stimulus timing. The resulting polar map shows that sharp borders can also be seen between phalanges of a single digit (Fig. 4B, arrows). Even though part of the proximal phalanx representation was hidden under a large vessel of the central sulcus, the proximal/middle phalangeal border is visible. A vessel map overlay of D2, D3, and D4 digit tips (Fig. 4C, solid lines) along with D3 proximal, middle, and distal phalanx borders (Fig. 4C, dotted lines), based on non-vessel-masked magnitude maps, reveals differences between D3 distal phalanx stimulation between the two experiments. Specifically, the phalangeal border of low magnitude between middle and distal phalanx are only seen

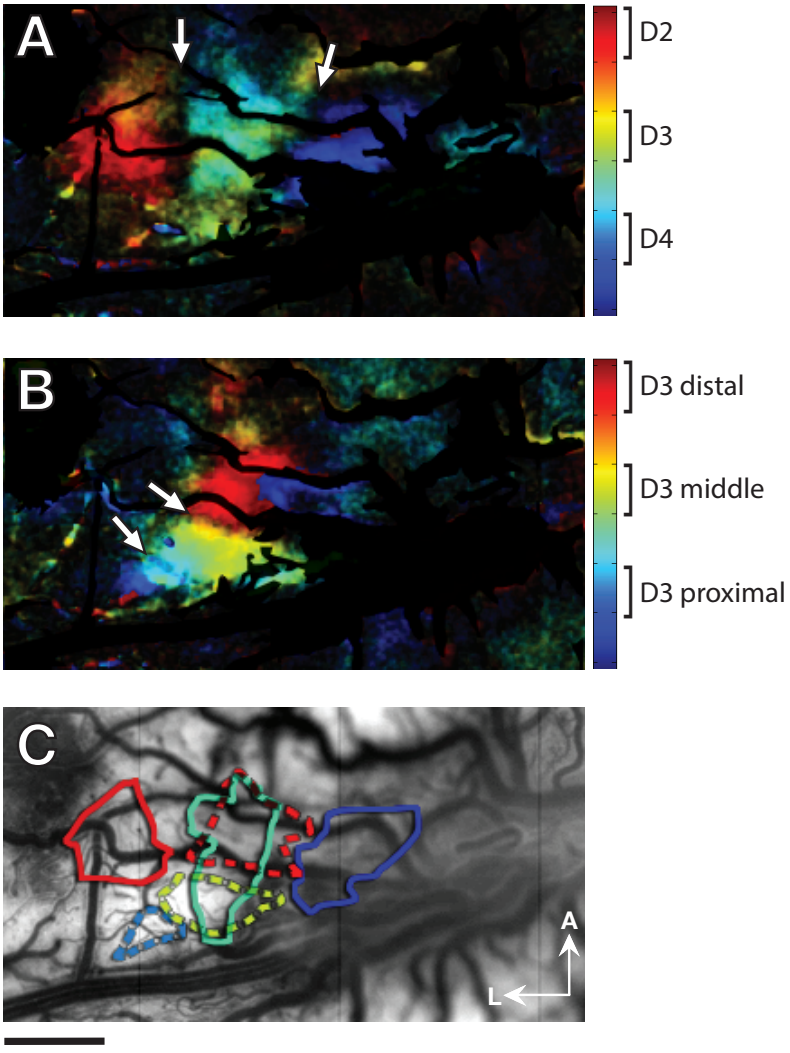

Figure 4. Polar maps illustrating between and within digit somatotopy. A. Polar maps showing the somatotopy of D2, D3, and D4. Arrows point to distinct borders between the digit representations. B. Polar map showing the somatotopy of the distal middle and proximal phalanx of D3. Arrows point to borders between the digit representations. C. Outlines of the between (solid lines) and within (dotted lines) digit activations overlaid on a blood vessel map. Note that the D3 stimulation of the distal phalanx from A, outlined in aqua green, extends into the representation of the middle phalanx. Scale bar = 1 mm. M = medial. A = anterior.

when stimulating both phalanges in the same experiment, whereas in the multidigit paradigm the D3 distal phalanx response spreads freely down the middle phalanx without any demarcation between phalanges. The sharp borders of signal dropout may demonstrate functional borders between competing signals, and should be useful for somatotopic mapping.

Digit selectivity indicated complex digit representation

Study of different harmonic components of the Fourier decomposition can be used to infer functional properties of tactile responses in the image. Using a Fourier imaging approach, with a properly constructed paradigm, it is possible to functionally interpret differences in the ratios of the magnitudes of the principal frequency vs harmonic frequencies. For example, in a study of visual cortical responses to a moving light bar scanned across the visual field, calculation of the ratio of the second and first harmonic of response has been used to demonstrate receptive field size differences between areas 17 and 18 (Vanni et al., 2010b). Here, we use a similar technique to measure the degree of digit selectivity across different cortical areas in SI. Digit selectivity can be measured by determining how strongly an area responds to only to a single digit. In this experiment, two adjacent digits were sequentially stimulated for 3s with 3s ISIs. Pixels responding to a single digit would show high magnitude at the principal frequency, 0.083 Hz, while pixels responding to both digits would show high magnitude at the second harmonic, 0.166 Hz. As an index of digit selectivity at each pixel, we divided the principal frequency magnitude by its second harmonic frequency magnitude. High digit selectivity would lead to large digit selectivity ratios.

Fig 5A is a vessel map of area 3b and area 1 in squirrel monkey cortex. The digit selectivity map (Fig. 5B) is shown as a heat map, with more digit-selective areas colored more red and less digit-selective areas colored more blue. All pixels have a ratio since magnitude is non-zero. We overlaid magnitude maps of the principal (Fig. 5C) and second (Fig. 5D) harmonics on the digit selectivity map in order to visualize the digit selectivity of only digit-activated areas. In areas activated at the principal frequency (Fig 5C), namely the representations of the D2 and D3 fingertips in areas 3b and 1, there was a common trend: a gradient of lower to higher digit selectivity from the adjacent border between digits to the nonadjacent borders. The ranges of digit selectivity in the activated regions of area 1 were similar to that seen in area 3b. Areas activated at the second harmonic (Fig. 5D) were found largely in the regions between those activated at the principal frequency, with more response overlapping with principal frequency response in area 3b than in area 1. The second harmonic response in area 3b was located directly between the regions of activity for the principal frequency, whereas the second harmonic response in area 1 was patchy and extended proximally (anteriorly in Fig. 5D) along the digit representation. A distant patch near the D1 representation in area 1 suggests that these patches could respond to non-adjacent digits as well. Second harmonic activity exists in the regions of magnitude dropout in the principal frequency for both areas 3b and 1. This suggests that the sharp magnitude borders at the principal frequency are actually areas activated by both digits.

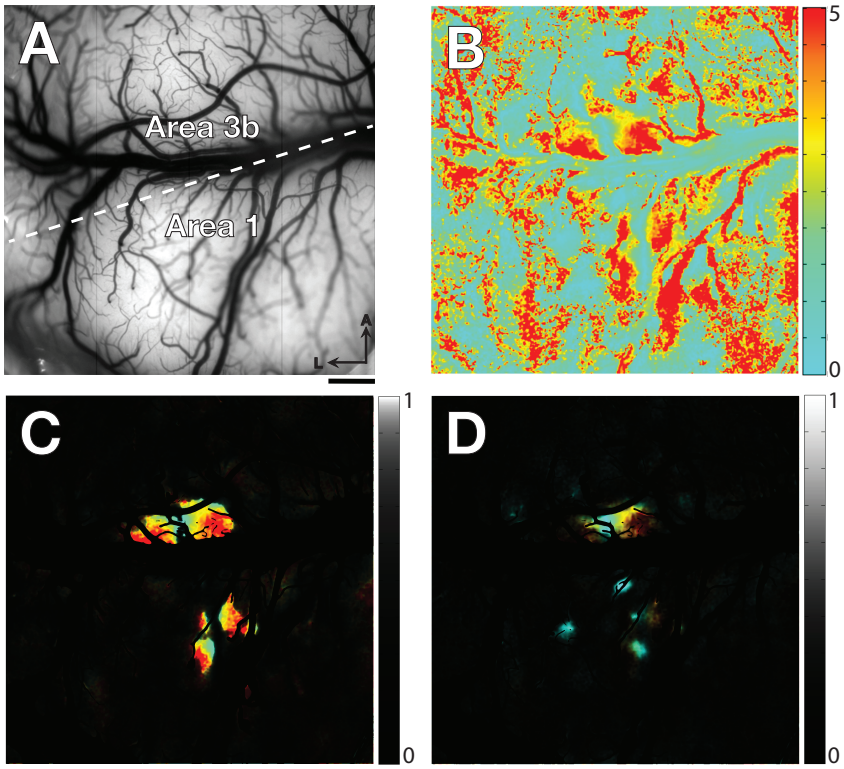

Figure 5. Areal digit selectivity revealed by analyzing the harmonics. A. Blood vessel map of the imaging field of view. B. Harmonic ratio map showing digit selectivity as a heat map. The principal frequency magnitude at each pixel was divided by its second harmonic frequency magnitude. Red: principal frequency (digit selective) >> second harmonic (multidigit responsive). Blue: second harmonic >> principal frequency. C. Principle frequency magnitude map overlaid on harmonic ratio map (B). D. Second harmonic magnitude map overlaid on harmonic ratio map (B). Note that regions activated at the second harmonic (multidigit responsive) were mostly found in between the regions activated at the principal frequency (digit selective). Scale bar = 1 mm. M = medial. A = anterior.

Signal to noise images reveal significance

Typical Fourier image analysis uses magnitude to show which areas are activated, but it remains unclear just how significant this activation really is. To obtain a better idea of the statistical significance of our signal maps, we determined the signal to noise ratio (SNR) at every pixel at the stimulation frequency. We first determined the noise level at the stimulus frequency by smoothing the magnitude spectrum after excluding the target frequency from the calculation of the smoothed waveform (see Fig. 1C-E, red lines). We then divided the signal magnitude at the target frequency by the estimated noise to obtain the SNR. Using this value, we constructed a new activation map based on the SNR and combined that with the existing phase map to make a new polar map. In order to show only significant values, a magnitude of 2.5 times the noise floor was set as the threshold baseline criteria.

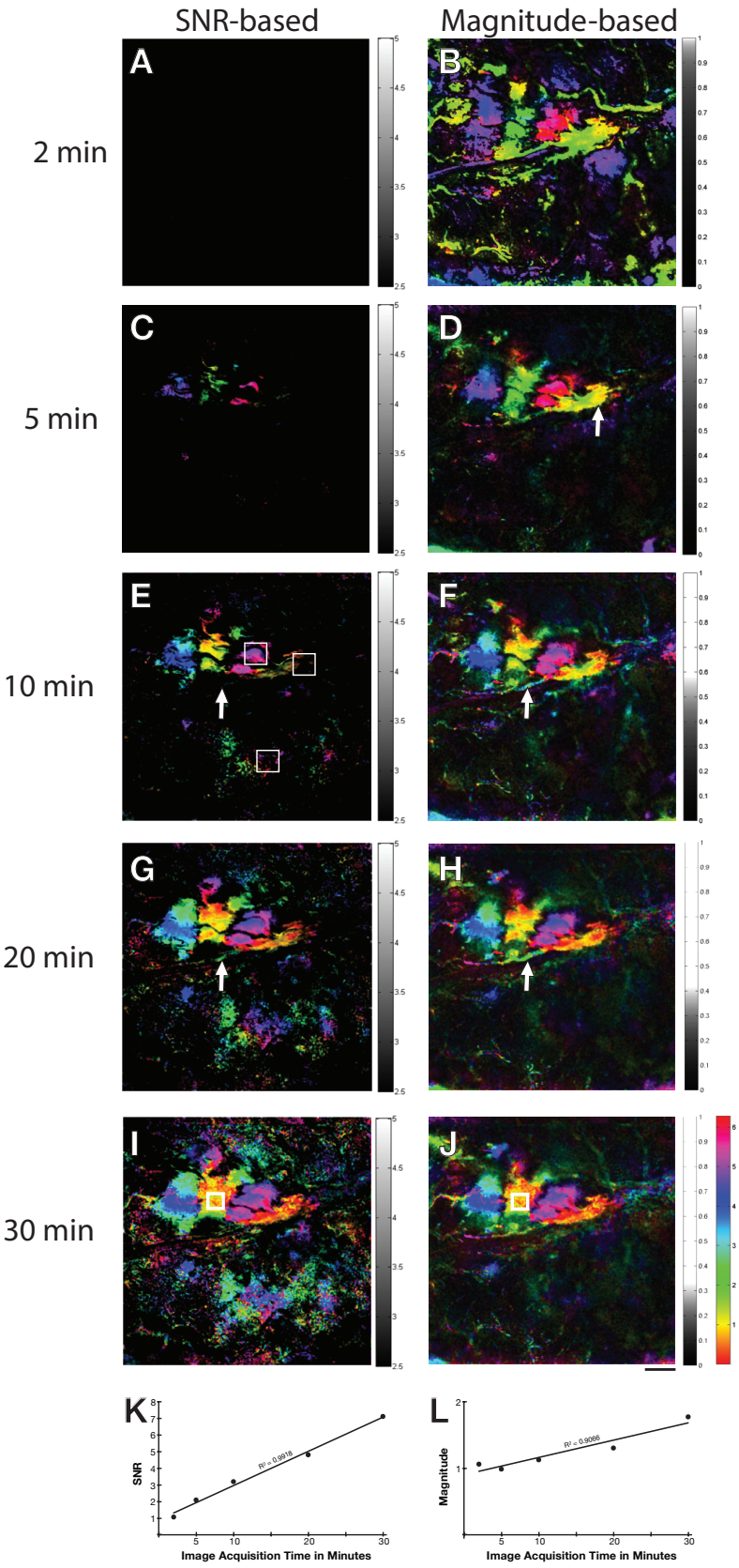
SNR-based
Magnitude-based
2 min
5 min
10 min
20 min
30 min
A
B
C
D
E
F
G
H
I
J
K
L
SNR
Magnitude
Image Acquisition Time in Minutes
Image Acquisition Time in Minutes

Figure 6. Effect of imaging duration on SNR-based and magnitude-based polar maps. For an imaging experiment of 30 min with D2, D3 and D4 stimulation, SNR-based polar maps (A, C, E, G, I) and magnitude-based polar maps are compared for 2 (A, B), 5 (C, D), 10 (E, F), 20 (G, H), and 30 (I, J) minutes of imaging. Arrow points to location of blood vessel. K. Amplitude of the SNR for an ROI in area 3b (box in I) as a function of image acquisition time. L. Magnitude of the principal component for an ROI in area 3b (box in L) as a function of image acquisition time. Boxes in E are ROIs for Fig. 1C-E. Scale bar = 1 mm.

As part of the motivation of this approach is to permit faster data acquisition, we wanted to examine how much time is needed to achieve good SNR. To do this, we acquired data for different periods of time (2, 5, 10, 20, and 30 minutes) and compared the SNR obtained at each duration. We also compared the SNR-based polar maps to magnitude-based polar maps for imaging runs at each duration (Fig. 6). With two minutes of imaging (10 period repetitions), SNR-based maps showed no significant signal (Fig. 6A), whereas magnitude-based maps showed signal for the three digits in area 3b as well as scattered signal in many regions that do not appear to be related to the tactile response (Fig. 6B). The magnitude in these unrelated regions is attributable to high random noise. After 5 minutes of imaging (25 period repetitions), SNR-based maps showed patchy activity for the three stimulated digit regions (Fig. 6C), whereas the magnitude-based maps showed signal restricted to three well-defined areas of digit stimulation, along with a few blood vessel regions (Fig. 6D). The strongest of these vessel artifacts arose from the large vessels emanating from the central sulcus (Fig. 6D arrow). With 10 minutes of imaging (50 period repetitions), SNR-based maps showed three discrete digit-activated areas in area 3b (upper half of Fig. 6E)) as well as activity in area 1 (lower half of Fig. 6E). Notably missing from the SNR-based map were significant vessel artifacts. The magnitude maps, by contrast, looked similar to the 5 minute maps, but showed more vessel artifacts. Arrows in Fig. 6E-F demonstrate the artifacts in magnitude-based polar maps that did not appear in SNR-based polar maps. Furthermore, magnitude maps only showed faint activity in area 1 that could easily be overlooked. After 20 minutes of imaging (100 period repetitions), the SNR-based map showed at least two digit-activated areas in area 1, but also began to show signs of vessel artifact (Fig. 6G). Magnitude-based maps showed no perceptible improvements over 10 minute maps (Fig. 6H). After 30 minutes of imaging (150 period repetitions), the SNR-based map revealed a large number of pixels with high SNR (Fig. 6I). This could be because the noise floor decreased enough for poorly activated regions to gain significance. The magnitude-based map demonstrated no perceptible improvements over the 20 or 10 minute maps (Fig. 6J). From a region of interest within area 3b, measurements of SNR showed a linear increase of SNR with longer acquisition times (Fig. 6K). For a well-activated region such as area 3b, 10 minutes of acquisition time was long enough to reach significance above an SNR of 2.5. Magnitude, however, showed a much smaller linear increase over increasing imaging times (Fig. 6L). Therefore, the reduction in noise over longer imaging durations accounts for most of the rise in SNR.

Comparison to standard mapping

To compare the digit-tip somatotopic map acquired by Fourier OIS with those obtained with episodic OIS and electrophysiological methods, we conducted episodic optical imaging using the same 12 s stimulus sequence. Area 3b activations for digits D1, D2, and D3 can be seen as dark regions in Fig 7A, B, C respectively. Digit D1 (Fig. 7A), the first digit in the sequence, produced a larger area of activation than the others that followed in close temporal proximity. In a Fourier OIS experiment with the same stimuli presented in sequence, the three digit-activated areas are seen (Fig. 7D). An overlay of activated digit areas from the episodic and Fourier images over a blood vessel map showed that the two imaging methods produce consistent digit topography (Fig. 7E). However, Fourier OIS provided a sharp phase border between digits D2 and D3, whereas episodic OIS showed overlap between the two activations. When compared with the receptive fields from electrophysiological penetrations, Fourier OIS correctly identified two D3 penetrations as being D3-exclusive that episodic OIS left ambiguous between D2 and D3 responses. Overall, Fourier OIS provides comparable digit topography to episodic OIS, but sharper digit borders in cases of overlapping responses between adjacent digits.

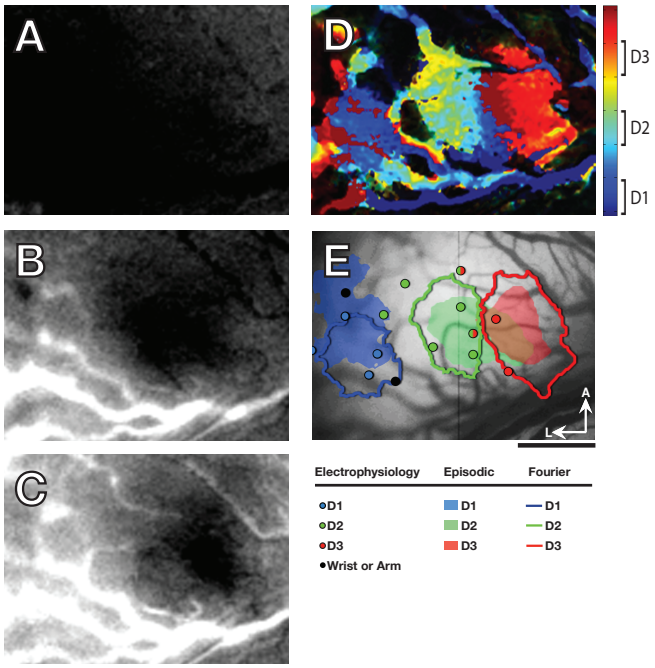

Figure 7. Consistency of across maps across methods. A-C. Episodic optical imaging using a 12 s stimulus sequence revealed peak activation maps of (A) D1, (B) D2, and (C) D3 activation. Area 3b activations for the digits are seen as dark regions. Intense white and black blood vessel artifacts in these images can be common in episodic imaging. D. Polar map from a continuous 10 min imaging experiment using the same stimulation sequence. E. Overlay of activated digit areas from the episodic (solid) and Fourier images (outlines) along with limit electrophysiological receptive field mapping on a blood vessel map. Scale bar = 1 mm. M = medial. A = anterior.

Chapter IV

Discussion

This study demonstrates the applicability of Fourier OIS in squirrel monkey primary somatosensory cortex. Finger topography, both across and along fingers, was successfully mapped in area 3b using the Fourier approach and was consistent with conventional episodic image acquisitionmethods. Phase lag correction was demonstrated using a single, periodic stimulus that simplifies the calculations required. Areas 1 and 3b were determined to have interdigit areas of overlapping response, leading to a clear border between stimulated areas in magnitude maps. Perhaps most significantly, signal to noise ratio maps were developed to visualize the significance of cortical responses, but also demonstrated a higher sensitivity to regions with a smaller response.

Animal Model

Squirrel monkeys are shown here to be good models for Fourier OIS. Heart rates are fast enough that there is little possibility of contamination of stimulation frequencies. As artificial respiration is standard for anesthetized procedures in these animals, respiration frequencies and its harmonics are easily avoided. Furthermore, most of the SI hand representation lies on the surface of the brain, making it ideal for imaging. Squirrel monkey SI does present certain challenges not typically encountered in other areas. Because of the termination of the central sulcus near the hand representation in SI resulting in multiple large surface vessels, and because most tactile stimuli are not applied to the entire sensory surface represented in the field of view, visible vascular artifacts are found both inside and outside the stimulated representations. These can be dealt with either with vessel masking or, to a lesser extent, with SNR analysis. Vascular artifacts are also found in episodic OIS, even after many averages, so their contribution in Fourier imaging is not a regression from prior methods.

Phase Correction

Stimulus reversal for phase correction relies on the cortical response being independent of stimulus order. This assumption has been validated across visual cortex in cats and rodents (Cang et al., 2005; Kalatsky and Stryker, 2003; Sato and Stryker, 2008), and auditory cortex in rats (Kalatsky et al., 2005). However, it has been reported that ferret auditory cortex responses are dependent on stimulus order (Nelken et al., 2004). Our study demonstrates the validity of stimulus reversal for phase correction in squirrel monkey SI, but also demonstrates a method of phase correction that does not assume an independence of stimulus order. This technique is well suited to squirrel monkey SI due to a restricted response area from mechanical stimulation of a small patch of skin. This approach may also prove useful in visual cortical models if a restricted spot size is used (Kalatsky, 2009).

Sharp Magnitude Borders

The current study found sharp magnitude borders at the principal stimulation frequency between digit representations in multi-digit stimulation. This bears a striking resemblance to interdigit septal regions previously reported in myelin stained tissues (Jain et al., 1998). However, sharp borders between phalanges in intra-digit stimulation are not supported by the anatomy. Furthermore, the intra-digit stimulation borders did not appear when only the fingertip was stimulated. Instead, the activation from the fingertip spread down beyond this border with no sign of the sharp border seen in the inter-digit condition. Insight into this discrepancy comes from the two-digit stimulation paradigm with harmonic analysis, wherein digit selectivity measures and differences between magnitude distribution demonstrate inter-digit regions of response overlap. The fall in magnitude at the principal frequency is explained with a rise in magnitude at the second harmonic frequency. The magnitude border thus indicates the area in which the two competing stimuli evoke about the same size of response. This is similar to findings in visual cortex, where the center of pinwheels have lower magnitude than the spokes of the pinwheels, as the center is activated equally by different orientations (Jha et al., 2005; Vanni et al., 2010a; Zepeda et al., 2004). While in pinwheels this characteristic of the analysis offers little benefit for viewing the overall topography, it is very useful for defining functional somatotopic borders in SI.

Digit selectivity

Digit selectivity analysis revealed similar patterns in areas 3b and 1. Both regions displayed highly digit-selective regions, with regions of lower digit selectivity between digits. Area 3b is emerging from its classical role, in which neurons' receptive fields are restricted to a single digit (DiCarlo et al., 1998; Sur et al., 1982). The current study supports other recent studies that described multi-digit influence in Area 3b (Chen et al., 2003; Lipton et al., 2010; Reed et al., 2008; 2010a; 2010b; Thakur et al., 2012). Area 1 may need adjustments to its classical role as well, as the digit selectivity analysis demonstrates a highly digit-selective region within each digit representation. This supports anatomical findings of homotopic projections from area 3b to area 1 (Négyessy et al., 2013).

SNR maps

The development of new statistical measures of significance in Fourier imaging is important, because within experiment variance is difficult to measure. Others have used correlation methods to measure the variance of orientation and direction maps in vision, but these require comparisons across multiple experiments (Kalatsky, 2009; Vanni et al., 2010a). As for the significance of the size of the response, other measures have been used. Magnitude maps have been a popular measure, despite not accounting for variance (Cang et al., 2005; Kalatsky et al., 2005; Kalatsky and Stryker, 2003; Sato and Stryker, 2008; Vanni et al., 2010a). Others broke a continuous signal into periods and generated measures of variance that way (Nelken et al., 2004; 2008; Sornborger et al., 2005). The current study demonstrates the potential of signal to noise ratio maps to determine significant strength of activation. These maps also show increased sensitivity to areas activated at low magnitudes. Obtaining significance at an SNR of 2.5

may require a longer imaging period, but as demonstrated in this study, it can make the difference between studying the response in a cortical area or just glancing over it. It is also possible to change the threshold of the SNR maps if a different level of significance is desired.

Future applications

One of the overarching goals of this project was to develop a rapid method of imaging with robust mechanisms for removing noise. The intended applications would be awake, behaving primate OIS as well as intraoperative human OIS. Both preparations generate much more noise than an anesthetized primate preparation. Furthermore, time is much more of a constraint in intraoperative human OIS, where imaging time is usually less than 20 minutes. A group recently published details for human Fourier OIS, demonstrating the method's clinical efficacy in identifying somatosensory cortex (Meyer et al., 2013; Oelschlägel et al., 2013; Sobottka et al., 2013a; 2013b). However, this group used median or radial nerve stimulation without phase encoding. Although their technique could identify the postcentral gyrus, it is not robust enough to map somatotopy. Further work should be done to bring a full implementation of Fourier OIS to human studies, such that both clinical and research interests could be gleaned from the same dataset.

With Fourier OIS established for primate somatotopy, the door is open for studies of other features with functional organization. Tactile receptor modality is an obvious candidate, as evidence indicates there is a topography for sustained, rapidly adapting and pacinian response (Sur et al., 1984; Friedman et al., 2004). However, continuously varying features, such as orientation and direction, take the greatest advantage of Fourier OIS, and have been studied using the method in cat and rodent visual cortex with Fourier methods (Kalatsky and Stryker, 2003; Vanni et al., 2010a). However, as yet, it is unknown whether tactile orientation and direction are organized in feature maps in primates.

There have been reports of a small population of neurons in area 2 that respond preferentially to different moving tactile orientations (Hyvärinen and Poranen, 1978; Warren et al., 1986); Pei, unpublished data). However, a few recent studies have shown that around 30-50% of neurons in Areas 3b and 1 respond with specificity to stimulus orientation (Bensmaia et al., 2008; DiCarlo and Johnson, 2000). This suggests that orientation processing is an important role of these areas. Direction has been studied with optical imaging in primate visual cortex, where a pinwheel map of direction was found in V2 thick and pale stripes (Lu et al., 2010). In the tactile modality, electrophysiological evidence shows that there are more direction-selective neurons in Area 1 than in Area 3b (Warren et al., 1986; Pei et al., 2010). Area 1 direction-selective neurons respond better than Area 3b direction-selective neurons to a broad category of stimuli, including scanned oriented bars, pseudorandom dot patterns, random dot patterns, and oriented plaids (Bensmaia et al., 2008; Pei et al., 2011; 2010). While direction preference in Area 3b neurons probably arises from their dynamic spatiotemporal receptive field structure, Area 1 neurons mostly lack infield inhibition and presumably obtain their direction selectivity from the combined input from multiple Area 3b neurons. Area 3b neurons do respond to local motion cues, but global motion

direction perception seems to be encoded by a population vector average in Area 1 (Pei et al., 2011). This could help to explain why the aperture illusion, whereby local motion cues initially drive direction perception followed by a corrected perception based on global motion cues, exists in somatosensation (Pei et al., 2008). The evidence so far strongly suggests a role of Area 1 in motion, particularly motion direction, making it urgent that we obtain a functional map of motion direction to guide future studies.

References

Bensmaia, S.J., Denchev, P.V., Dammann, J.F., Craig, J.C. and Hsiao, S.S. (2008) The representation of stimulus orientation in the early stages of somatosensory processing. *J Neurosci*, **28**, 776–786.

Blasdel, G.G. and Salama, G. (1986) Voltage-sensitive dyes reveal a modular organization in monkey striate cortex. *Nature*, **321**, 579–585.

Bonhoeffer, T. and Grinvald, A. (1991) Iso-orientation domains in cat visual cortex are arranged in pinwheel-like patterns. *Nature*, **353**, 429–431.

Boynton, G.M., Engel, S.A., Glover, G.H. and Heeger, D.J. (1996) Linear Systems Analysis of Functional Magnetic Resonance Imaging in Human V1. *J Neurosci*, **16**, 4207–4221.

Broca, P. (1861) Remarks on the Seat of the Faculty of Articulated Language, Following an Observation of Aphemia (Loss of Speech). *Broca's Region*, **6**, 330–357.

Cang, J., Kalatsky, V.A., Löwel, S. and Stryker, M.P. (2005). Optical imaging of the intrinsic signal as a measure of cortical plasticity in the mouse. *Vis Neurosci*, **22**, 685–691.

Chen, L.M., Friedman, R.M., Ramsden, B.M., LaMotte, R.H. and Roe, A.W. (2001) Fine-scale organization of SI (area 3b) in the squirrel monkey revealed with intrinsic optical imaging. *J Neurophysiol*, **86**, 3011–3029.

Chen, L.M., Friedman, R.M. and Roe, A.W. (2003) Optical imaging of a tactile illusion in area 3b of the primary somatosensory cortex. *Science*, **302**, 881–885.

Chen, L.M., Friedman, R.M. and Roe, A.W. (2009) Optical imaging of digit topography in individual awake and anesthetized squirrel monkeys. *Exp Brain Res*, **196**, 393–401.

Chen, L.M., Turner, G.H., Friedman, R.M., Zhang, N., Gore, J.C., Roe, A.W. and Avison, M.J. (2007) High-resolution maps of real and illusory tactile activation in primary somatosensory cortex in individual monkeys with functional magnetic resonance imaging and optical imaging. *J Neurosci*, **27**, 9181–9191.

DeYoe, E.A., Carman, G.J., Bandettini, P., Glickman, S., Wieser, J., Cox, R., Miller, D. and Neitz, J. (1996) Mapping striate and extrastriate visual areas in human cerebral cortex. *Proc Natl Acad Sci USA*, **93**, 2382–2386.

DiCarlo, J.J. and Johnson, K.O. (2000) Spatial and temporal structure of receptive fields in primate somatosensory area 3b: effects of stimulus scanning direction and orientation. *J Neurosci*, **20**, 495–510.

DiCarlo, J.J., Johnson, K.O. and Hsiao, S.S. (1998) Structure of receptive fields in area 3b of primary somatosensory cortex in the alert monkey. *J Neurosci*, **18**, 2626–2645.

Engel, S.A., Glover, G.H. and Wandell, B.A. (1997) Retinotopic organization in human visual cortex and the spatial precision of functional MRI. *Cereb Cortex*, **7**, 181–192.

Engel, S.A., Rumelhart, D.E., Wandell, B.A., Lee, A.T., Glover, G.H., Chichilnisky, E.J. and Shadlen, M.N. (1994) fMRI of human visual cortex. *Nature*, **369**, 525.

Ferrier, D. (1873) Experimental Researches in Cerebral Physiology and Pathology. *J Anat Physiol*, **8**, 152–155.

Friedman, R.M., Chen, L.M. and Roe, A.W. (2004) Modality maps within primate somatosensory cortex. *Proc Natl Acad Sci USA*, **101**, 12724–12729.

Friedman, R.M., Chen, L.M., and Roe, A.W. (2008) Responses of areas 3b and 1 in anesthetized squirrel monkeys to single- and dual-site stimulation of the digits. *Journal of Neurophysiology*, **100**(6), 3185–3196.

Hubel, D.H. and Wiesel, T.N. (1962) Receptive fields, binocular interaction and functional architecture in the cat's visual cortex. *J Physiol*, **160**, 106–154.

Hyvärinen, J. and Poranen, A. (1978) Movement-sensitive and direction and orientation-selective cutaneous receptive fields in the hand area of the post-central gyrus in monkeys. *J Physiol*, **283**, 523–537.

Jain, N., Catania, K.C. and Kaas, J.H. (1998) A histologically visible representation of the fingers and palm in primate area 3b and its immutability following long-term deafferentations. *Cereb Cortex*, **8**, 227–236.

Jha, S.K., Jones, B.E., Coleman, T., Steinmetz, N., Law, C.-T., Griffin, G., Hawk, J., Dabbish, N., Kalatsky, V.A. and Frank, M.G. (2005) Sleep-dependent plasticity requires cortical activity. *J Neurosci*, **25**, 9266–9274.

Kalatsky, V.A. (2009) Fourier Approach for Functional Imaging, in: Frostig, R.D. (Ed.), In Vivo Optical Imaging of Brain Function. CRC Press, Taylor & Francis Group, Boca Raton, FL, pp. 287–312.

Kalatsky, V.A., Polley, D.B., Merzenich, M.M., Schreiner, C.E. and Stryker, M.P. (2005) Fine functional organization of auditory cortex revealed by Fourier optical imaging. *Proc Natl Acad Sci*, **102**, 13325–13330.

Kalatsky, V.A. and Stryker, M.P. (2003) New Paradigm for Optical Imaging. *Neuron*, **38**, 529–545.

Lipton, M.L., Liszewski, M.C., O'Connell, M.N., Mills, A., Smiley, J.F., Branch, C.A., Isler, J.R., and Schroeder, C.E. (2010) Interactions within the hand representation in primary somatosensory cortex of primates. *J Neurosci*, **30**, 15895–15903.

Lu, H.D., Chen, G., Tanigawa, H. and Roe, A.W. (2010) A motion direction map in macaque V2. *Neuron*, **68**, 1002–1013.

Meyer, T., Sobottka, S.B., Kirsch, M., Schackert, G., Steinmeier, R., Koch, E. and Morgenstern, U. (2013) Intraoperative optical imaging of functional brain areas for improved image-guided surgery. *Biomedizinische Technik/Biomedical Engineering*, **58**, 225–236.

Mountcastle, V.B. (1957) Modality and topographic properties of single neurons of cat's somatic sensory cortex. *J Neurophysiol*, **20**, 408–434.

Nelken, I., Bizley, J.K., Nodal, F.R., Ahmed, B., King, A.J. and Schnupp, J.W.H. (2008) Responses of auditory cortex to complex stimuli: functional organization revealed using intrinsic optical signals. *J Neurophysiol*, **99**, 1928–1941.

Nelken, I., Bizley, J.K., Nodal, F.R., Ahmed, B., Schnupp, J.W.H. and King, A.J. (2004) Large-scale organization of ferret auditory cortex revealed using continuous acquisition of intrinsic optical signals. *J Neurophysiol*, **92**, 2574–2588.

Nelson, R.J. and Kaas, J.H. (1981) Connections of the ventroposterior nucleus of the thalamus with the body surface representations in cortical areas 3b and 1 of the cynomolgus macaque, (Macaca fascicularis). *J Comp Neurol*, **199**, 29–64.

Négyessy, L., Pálfi, E., Ashaber, M., Palmer, C., Jákli, B., Friedman, R.M., Chen, L.M. and Roe, A.W. (2013) Intrinsic horizontal connections process global tactile features in the primary somatosensory cortex: neuroanatomical evidence. *J Comp Neurol*, **521**, 2798–2817.

Oelschlägel, M., Meyer, T., Wahl, H., Sobottka, S.B., Kirsch, M., Schackert, G. and Morgenstern, U. (2013) Evaluation of intraoperative optical imaging analysis methods by phantom and patient measurements. *Biomedizinische Technik/Biomedical Engineering*, **58**, 257–267.

Paul, R.L., Goodman, H. and Merzenich, M. (1972a) Alterations in mechanoreceptor input to Brodmann's areas 1 and 3 of the postcentral hand area of Macaca mulatta after nerve section and regeneration. *Brain Res*, **39**, 1–19.

Paul, R.L., Merzenich, M. and Goodman, H. (1972b) Representation of slowly and rapidly adapting cutaneous mechanoreceptors of the hand in Brodmann's areas 3 and 1 of Macaca mulatta. *Brain Res*, **36**, 229–249.

Pei, Y.-C., Hsiao, S.S., Craig, J.C. and Bensmaia, S.J. (2010) Shape invariant coding of motion direction in somatosensory cortex. *PLoS Biol*, **8**, e1000305.

Pei, Y.-C., Hsiao, S.S., Craig, J.C. and Bensmaia, S.J. (2011) Neural mechanisms of tactile motion integration in somatosensory cortex. *Neuron*, **69**, 536–547.

Pei, Y.C., Hsiao, S.S. and Bensmaïa, S.J. (2008) The tactile integration of local motion cues is analogous to its visual counterpart. *Proc Natl Acad Sci*, **105**, 8130–8135.

Penfield, W. and Jasper, H.H. (1954) Epilepsy and the functional anatomy of the human brain. Little, Brown, Boston.

Piotrowska, N. and Winkler, P.A. (2007) Otfrid Foerster, the great neurologist and neurosurgeon from Breslau (Wrocław): his influence on early neurosurgeons and legacy to present-day neurosurgery. *J Neurosurg*, **107**, 451–456.

Pons, T.P., Garraghty, P.E., Friedman, D.P. and Mishkin, M. (1987) Physiological evidence for serial processing in somatosensory cortex. *Science*, **237**, 417–420.

Powell, T.P. and Mountcastle, V.B. (1959) Some aspects of the functional organization of the cortex of the postcentral gyrus of the monkey: a correlation of findings obtained in a single unit analysis with cytoarchitecture. *Bulletin of the Johns Hopkins Hospital*, **105**, 133–162.

Reed, J.L., Pouget, P., Qi, H.-X., Zhou, Z., Bernard, M.R., Burish, M.J., Haitas, J., Bonds, A.B. and Kaas, J.H. (2008) Widespread spatial integration in primary somatosensory cortex. *Proc Natl Acad Sci*, **105**, 10233–10237.

Reed, J.L., Qi, H.-X., Pouget, P., Burish, M.J., Bonds, A.B. and Kaas, J.H. (2010a) Modular processing in the hand representation of primate primary somatosensory cortex coexists with widespread activation. *J Neurophysiol*, **104**, 3136–3145.

Reed, J.L., Qi, H.-X., Zhou, Z., Bernard, M.R., Burish, M.J., Bonds, A.B. and Kaas, J.H. (2010b) Response properties of neurons in primary somatosensory cortex of owl monkeys reflect widespread spatiotemporal integration. *J Neurophysiol*, **103**, 2139–2157.

Sato, M. and Stryker, M.P. (2008) Distinctive features of adult ocular dominance plasticity. *J Neurosci*, **28**, 10278–10286.

Sereno, M.I., Dale, A.M., Reppas, J.B., Kwong, K.K., Belliveau, J.W., Brady, T.J., Rosen, B.R. and Tootell, R.B. (1995) Borders of multiple visual areas in humans revealed by functional magnetic resonance imaging. *Science*, **268**, 889–893.

Sobottka, S.B., Meyer, T., Kirsch, M., Koch, E., Steinmeier, R., Morgenstern, U. and Schackert, G. (2013a) Intraoperative optical imaging of intrinsic signals: a reliable method for visualizing stimulated functional brain areas during surgery. *J Neurosurg*, **119**(4), 853-863.

Sobottka, S.B., Meyer, T., Kirsch, M., Koch, E., Steinmeier, R., Morgenstern, U. and Schackert, G. (2013b) Evaluation of the clinical practicability of intraoperative optical imaging comparing three different camera setups. *Biomedizinische Technik/Biomedical Engineering*, **58**, 237–248.

Sornborger, A., Yokoo, T., Delorme, A., Sailstad, C. and Sirovich, L. (2005) Extraction of the average and differential dynamical response in stimulus-locked experimental data. *J Neurosci Methods*, **141**, 223–229.

Sur, M., Nelson, R.J. and Kaas, J.H. (1982) Representations of the body surface in cortical areas 3b and 1 of squirrel monkeys: comparisons with other primates. *J Comp Neurol*, **211**, 177–192.

Sur, M., Wall, J.T., and Kaas, J.H. (1984) Modular distribution of neurons with slowly adapting and rapidly adapting responses in area 3b of somatosensory cortex in monkeys. *Journal of Neurophysiology*, **51**(4), 724–744.

Thakur, P.H., Fitzgerald, P.J. and Hsiao, S.S. (2012) Second-order receptive fields reveal multidigit interactions in area 3b of the macaque monkey. *J Neurophysiol*, **108**, 243–262.

Ts'o, D.Y., Roe, A.W. and Gilbert, C.D. (2001) A hierarchy of the functional organization for color, form and disparity in primate visual area V2. *Vision Res*, **41**, 1333–1349.

Vanni, M.P., Provost, J., Casanova, C. and Lesage, F. (2010a) Bimodal modulation and continuous stimulation in optical imaging to map direction selectivity. *Neuroimage*, **49**, 1416–1431.

Vanni, M.P., Provost, J., Lesage, F., and Casanova, C. (2010b) Evaluation of receptive field size from higher harmonics in visuotopic mapping using continuous stimulation optical imaging. *J Neurosci Methods*, **189**, 138–150.

Warren, S., Hämäläinen, H.A. and Gardner, E.P. (1986) Objective classification of motion- and direction-sensitive neurons in primary somatosensory cortex of awake monkeys. *J Neurophysiol*, **56**, 598–622.

Zepeda, A., Arias, C. and Sengpiel, F. (2004) Optical imaging of intrinsic signals: recent developments in the methodology and its applications. *J Neurosci Methods*, **136**, 1–21.